Journal of Materials Chemistry A

ROYAL SOCIETY OF CHEMISTRY

PAPER

View Article Online
View Journal | View Issue

Cite this: J. Mater. Chem. A, 2020, 8, 22791

Flexible and additive-free organic electrodes for aqueous sodium ion batteries†

Liping Yang,[a] Pengyuan Wang,[b] Shangwei Zhang,[c] Yuanhao Wang,[d] Ling Zang,[e] Hui Zhu,[a] Jiao Yin *[a] and Hui Ying Yang *[f]

Received 25th July 2020
Accepted 11th October 2020

DOI: 10.1039/d0ta07267b

rsc.li/materials-a

Organic materials with redox activities are promising candidates for aqueous flexible sodium ion storage devices (AFSISDs) due to their mechanical flexibility and low dissolution in aqueous electrolytes. However, the advantages of organic electrodes are not fully exploited due to uncontrollable morphologies with sluggish electrochemical kinetics, and lack of deep understanding about the storage mechanism *via in situ* technologies. Herein, an interfacial self-assembly strategy is proposed to directly construct PTCDI nanofibers onto flexible ITO substrates by a binder-free approach. Combining *in situ* Raman spectroscopy and DFT calculations, the Na^+ storage mechanism based on an enolization reaction (–C=O ↔ –C–O–Na) of two carbonyl groups located in the *para* position of PTCDI is illuminated. Coupled with an activated carbon cathode, the organic AFSISD delivers an ultrahigh energy density of 83.8 W h kg^{-1} and a largely improved power density of 3.4 kW kg^{-1}. The as-prepared organic nanofibers show a superior volumetric energy and high power density (*i.e.*, 7.1 mW h cm^{-3} and 289.7 mW cm^{-3}). This work opens up new horizons for a wide variety of flexible electronics based on organic electrode materials in aqueous neutral electrolytes.

1. Introduction

The growing demand for wearable electronic devices promotes the urgent need for flexible energy storage devices with high energy density, excellent cyclicality and a long life span.[1,2] Sodium-ion batteries (SIBs) have been recognised as one promising alternative to conventional lithium-ion batteries (LIBs) owing to the abundant sodium resources.[3,4] Searching for flexible suitable electrode materials with high reversible capacity and fast Na^+ ion transport kinetics is vitally important and challenging. Using aqueous flexible sodium ion storage devices (AFSISDs) has been featured as an attractive approach because of the integrative device advantages. In the construction of AFSISDs, the aqueous electrolytes are considered to be inherently safer, cheaper and more environmentally friendly than their conventional organic counterparts.[5,6] Organic electrodes have been intensively explored as promising candidates for sodium storage, due to their low cost, abundant resources, excellent structural adaptability and mechanical flexibility. However, most of the organic electrodes suffer from poor electrical conductivity and high dissolution in organic electrolytes.[7,8] Therefore, effective organic electrodes with high capacity and stability have attracted a significant amount of research interest. To make an effective configuration of AFSISDs, numerous attempts have been proposed to embed organic active materials in flexible conductive substrates, such as carbon nanofibers, carbon nanotubes, graphene derivatives and carbon textiles.[9–11] However, the mass loading of organics is relatively low in these strategies, which ultimately limited the practical energy density, especially the volumetric energy density. It is highly desirable to develop novel strategies to construct flexible electrodes with a high mass loading of organic active materials.

As a promising organic electrode material, perylene tetracarboxylic diimide (PTCDI) has demonstrated excellent electrochemical performances for Li^+/Na^+/K^+ ion storage, because of its functional carbonyl groups with the reversible enolization –C=O ↔ –C–O–M mechanism.[12–14] However, the low electrical conductivity and high dissolution in organic electrolytes result in unsatisfactory rate capability, poor cycle stability and

[a]Laboratory of Environmental Sciences and Technology, Xinjiang Technical Institute of Physics & Chemistry, Key Laboratory of Functional Materials and Devices for Special Environments, Chinese Academy of Sciences, Urumqi 830011, China. E-mail: yinjiao@ms.xjb.ac.cn

[b]School of Physical Science and Technology, Xinjiang University, Urumqi 830046, PR China

[c]UFZ Department of Ecological Chemistry, Helmholtz Centre for Environmental Research, Permoserstraße 15, 04318 Leipzig, Germany

[d]SUSTech Engineering Innovation Center, School of Environmental Science and Engineering, Southern University of Science and Technology, China

[e]Nano Institute of Utah, Department of Materials Science and Engineering, University of Utah, Salt Lake City, Utah 84112, USA

[f]Pillar of Engineering Product Development, Singapore University of Technology and Design, 8 Somapah Road, Singapore 487372, Singapore. E-mail: yanghuiying@sutd.edu.sg

† Electronic supplementary information (ESI) available. See DOI: 10.1039/d0ta07267b

eventually limited its practical applications.[15–17] Even though the polymerization strategy has been proposed to circumvent the dissolution phenomena, the conductivity of PTCDI for ion/electron transfer deteriorated inevitably. In addition, such an attempt cannot tailor the mass loading of PTCDI onto a substrate, failing in enhancing the energy density of devices.[16–18] Recently, we have developed an *in situ* assembly strategy to efficiently deposit PTCDI nanofibers with optimized charge transport along the long axis on the ITO surface.[19,20] More impressively, the procedure of layer by layer stacking facilitates the controllable formation of homogeneous and compact nanofibrous PTCDI networks. Inspiringly, we creatively deposit PTCDI nanofibers on a soft ITO support *via* a molecular self-assembly strategy to form an unique flexible electrode with enhanced electrochemical performance such as larger specific capacity, higher rate capability and a long cycling life due to the following advantages: (a) increased intra/intermolecular charge transport along the long axis of PTCDI nanofibers mediated by the effective intermolecular electron delocalization and short diffusion distance for interfacial ions owing to the tightly ordered molecular self-assembly;[19,20] (b) sufficient exposed surface with abundant active sites for charge storage and a strong adhesive force to anchor onto the substrate without any binder and conductive additives; (c) a good insolubility of the studied PTCDI in aqueous solution (for example: neutral sulfate solution and sulfuric acid solution) resulting in low shedding/dissolution probability of PTCDI nanofibers during the cycle test.[20,33] Furthermore, the reversible redox mechanism of PTCDI nanofibers during the charge/discharge process is revealed *via* the integration of *in situ* Raman characterization and DFT calculations. Taking advantage of the safety of neutral aqueous electrolytes, excellent ionic conductivity, and the efficient dissolution suppression of PTCDI during charge/discharge cycling, we designed an AFSISD in which flexible PICDI nanofibers and an activated carbon film are used as the anode and cathode respectively. The fabricated AFSISD delivers a high energy density, power density and satisfactory cycling stability, outperforming nearly all previous aqueous hybrid devices. This study illustrates a facile self-assembly strategy to construct high-performance flexible electrodes using organic materials, providing a new method for the construction of wearable flexible electronic devices.

2. Experimental section

2.1. Synthesis of the PTCDI D–A molecule

The PTCDI molecule (2,9-bis[1-[(1-methyl-4-piperidyl)methyl]]-3,4,9,10-perylene tetracarboxylic diimide) was synthesized following our previously reported literature as shown Fig. S1.†[19]

2.2. Synthesis of activated carbon (AC)

Coconut shell charcoal (CSC, from AC Company in Jiangsu) and KOH (mass ration, CSC : KOH = 1 : 4) were mixed as the carbon source and activator respectively, and activated at 800 °C for 1 h. When cooling down, it was washed with 2 M HCl and deionized water respectively, to eliminate any metal residues totally. Finally, the obtained sample was dried at 80 °C for 24 h and labeled AC.

2.3. Preparation of PTCDI D–A nanofibers

PTCDI nanofibers were formed by a solvent-vapor diffusion process, resulting in interfacial self-assembly on the surface of indium tin oxide (ITO) films, which served as the current collector. Specifically, a solid screw-cap containing 0.6 × 0.6 cm^2 ITO films was placed in a crystallizing dish, and 40 mL of methanol was injected to allow the screw cap to float on the methanol liquid. Then, 80 μL PTCDI solution (1.0 mM PTCDI solution in chloroform) was slowly drop-cast onto the ITO surface, rapidly sealed and transferred to an oven at 30 °C for 24 h. Finally, the nanofibers were dried in a vacuum oven at 50 °C for 60 min.

2.4. Material characterization

The morphology, microstructure, and functional groups of PTCDI nanofibers were characterized by SEM (Philips XL 30 instrument and a JEOL JSM-6700F microscope), FTIR (Bruker Vertex 70 FT-IR spectrometer) and micro-Raman spectroscopy (LabRAM HR JY-Evolution, 532 nm). The porous structure of AC was characterized by using nitrogen adsorption/desorption isotherms, which were recorded at 77 K with a Quadrachrome adsorption instrument. Before analysis, the samples were degassed at 200 °C for 24 h. The surface area was calculated according to the Brunauer–Emmett–Teller (BET) method.

2.5. *In situ* Raman measurements

As can be seen from Fig. S3,† the test system mainly contains three parts. The computer is connected to the electrochemical workstation which is connected to the sample tank for cyclic voltammetry testing. Raman spectroscopy was used to real-time record the changes of chemical bonds in the whole reaction process.

2.6. Electrode fabrication

The PTCDI nanofiber electrode was prepared as described in the preparation of PTCDI nanofibers. The weight of PTCDI nanofibers is 0.05 mg and the active area is 0.36 cm^2. The AC electrode was prepared by mixing the active material (80 wt% AC), conductive carbon (10 wt% Super P), and PVDF dissolved in *N*-methyl-2-pyrrolidone (NMP) (10 wt% PVDF). The mixed slurry was uniformly cast over the ITO films. The loading weight of AC is 0.8 mg and the active area is 0.36 cm^2. The obtained electrodes were dried under vacuum at 50 °C for 180 min.

2.7. Electrochemical tests

The electrochemical measurements were carried out on an electrochemical workstation (CHI760E, Chenhua, China). The electrochemical tests of half-cells were carried out using a three-electrode cell with platinum as the counter electrode and Ag/AgCl as the reference electrode. 1 M Na_2SO_4 solution was used as the electrolyte. Impedance spectra were recorded in the 0.1 Hz to 100 kHz frequency range with a 5 mV AC amplitude.

Cyclic voltammetry was conducted in the −0.8 to 0.5 V range at increasing sweep rates from 1 to 1000 mV s^{-1}. Galvanostatic charge/discharge cycling was performed in the −0.9 to 0.1 V range at current densities in the 0.2–9.0 A g^{-1} range. The specific gravimetric capacitance (C_g) and areal capacitance (C_s) based on the galvanostatic discharge for the three electrode system are calculated using eqn (1) and (2):

$$C_g = \frac{I \times \Delta t}{M \times \Delta U} \quad (1)$$

$$C_s = \frac{I \times \Delta t}{s \times \Delta U} \quad (2)$$

where I is the discharge current (A), M is the mass of the active materials ($M_{PTCDI} = 0.05$ mg) in the electrode (g), s is the areal of active materials ($s_{PTCDI} = 0.36$ cm^2), ΔU (V) stands for the potential window within the discharge time Δt (s) after the ohmic drop. Full cell (PTCDI//AC) characterization was carried out in a two-electrode cell, with PTCDI nanofibers as the negative electrode combined with AC as the positive electrode with equivalent capacity. Both electrodes were submerged in a 1 M Na_2SO_4 aqueous electrolyte. Cyclic voltammetry was conducted in the 0–1.5 V range at increasing sweep rates from 1 to 100 mV s^{-1}. Galvanostatic charge–discharge experiments were carried out in the 0–1.46 V range at current densities in the 0.03–2.4 A g^{-1} range. The specific capacity ($C_{full\text{-}g}$ and $C_{full\text{-}s}$) and current density were calculated based on the total mass of both PTCDI and AC units in the full cell using eqn (3) and (4):

$$C_{full\text{-}g} = \frac{2 \times I \times \Delta t}{M \times \Delta U} \quad (3)$$

$$C_{full\text{-}s} = \frac{2 \times I \times \Delta t}{S_{total} \times \Delta U} \quad (4)$$

where S_{total} is the total areal of active materials ($S_{total} = 0.72$ cm^2). The specific energy density (E, W h kg^{-1}) and specific power density (P, W kg^{-1}) of the full cell (PTCDI//AC) were calculated by using eqn (5) and (6):

$$E = \frac{C_{full\text{-}g} \times \Delta U^2}{2 \times 3.6} \quad (5)$$

$$P = \frac{E \times 3600}{\Delta t} \quad (6)$$

where ΔU is the operating voltage ($\Delta U = U_{max} - IR$ drop) and Δt (s) is the discharge time. Moreover, the volumetric energy density (E, mW h cm^{-3}) and volumetric power density (P, mW cm^{-3}) of the devices were obtained according to eqn (7) and (8):

$$P = \frac{\Delta U \times I}{2 \times V} \quad (7)$$

$$E = P \times t \quad (8)$$

where I (mA) is the applied current, V (cm^3) is the volume of the whole device (the areal and thickness of PTCDI//AC are about 0.6 × 0.6 cm^2 and 0.14 mm. Hence, the whole volume of the device is about 0.00504 cm^3), t (h) is the discharging time, and ΔU (V) is the voltage window of GCD.

2.8. Computational methodology

All density functional calculations covering geometry optimization and vibrational analysis were performed at the theoretical level of Beck's 3-parameter Lee–Yang–Parr (B3LYP) with the basis set Def2SVP as implemented in Gaussian 09 Rev. D01. All equilibrium geometries were confirmed by the absence of imaginary frequencies. The gas phase Gibbs free energy of sodium addition at 1 atm and 298 K was corrected with zero-point and thermal energies from the vibrational analysis. Table S3† shows the cartesian coordinates of various PTCDI molecules.

3. Results and discussion

3.1. Synthesis, structure and morphology characterization

Fig. 1a illustrates the schematic diagram for the fabrication of the flexible binder-free PTCDI electrodes. As shown, a cleaned ITO membrane which serves as a current collector is placed at the bottom of a shallow, wide, open container. Then the surface of the ITO film is covered with a certain amount of the PTCDI stock solution (1 mM in chloroform). After that, the container is moved into a sealed vessel which contains methanol (poor solvent for PTCDI). Finally, following the solvent exchange which is driven by the vapor diffusion of methanol, the PTCDI molecules self-assemble into a nano-fibrous framework to form electrodes *via* π–π molecular stacking forces gradually. As evidenced by SEM characterization in Fig. 1b, the as-prepared PTCDI nanofibers fully cover the surface of ITO, implying the success of this fabrication strategy. The detailed image shows that the diameter and length of the PTCDI nanofibers are about 300 nm and up to 10 micrometers, respectively. It is impressive that these thin nanofibers interconnect each other to form networks with a strong adhesion to the ITO substrate for efficient electron transfer. Additionally, this structural characteristic also reflects a large electrode/electrolyte interface and a shortened distance for sodium ion diffusion. Moreover, the structural evolution after the assembly process was also discovered by spectra technologies. It is observed that PTCDI nanofibers present higher relative intensities than the PTCDI molecule, supporting the occurrence of ordered molecular organization during assembly (Fig. 1c). In detail, besides the C–H in-plane bending vibrations (1300–900 cm^{-1}), the intensive absorption of C=C stretching at 1580 cm^{-1} and the strong C–N stretching at 1350 cm^{-1} indicate a large value of the dipole moment derivative. Impressively, the strong peaks at 1692 cm^{-1} and 1650 cm^{-1} can be ascribed to the antisymmetric in phase vibration and the out-of-phase symmetric stretching of C=O groups respectively, informing an abundant exposure of active sites for charge storage. Similarly, C=O, C=C, C–H, ring and ring radical stretching vibrations in PTCDI were also detected in Raman spectroscopy (Fig. 1d).[21,22] In short, all these structural characteristics indicate the successful self-assembly of PTCDI and the existence of C=O groups.

3.2. Electrochemical characterization of PTCDI nanofibers and mechanism exploration

To evaluate the electrochemical performance of PTCDI nanofiber electrodes, galvanostatic charge–discharge (GCD)

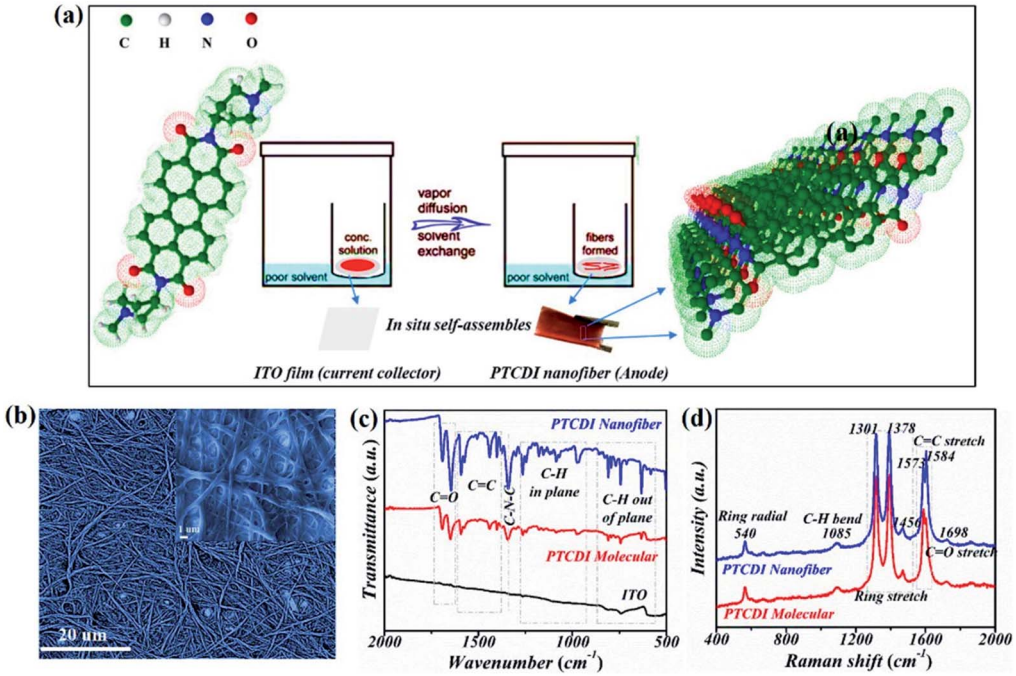

Fig. 1 (a) The schematic diagram for the fabrication of the flexible binder-free PTCDI electrodes. (b) SEM images of PTCDI nanofibers. (c) FTIR and (d) Raman spectroscopy of PTCDI.

measurements were performed in 1 M Na_2SO_4 aqueous solution with a three-electrode system. It is observed in Fig. 2a that the curves bend at ~−0.4 V in the charging process and the discharging lines below −0.5 V are bent, implying the participation of redox reactions which might be caused by the reversible transformation between –C═O and –C–O–Na. That is, an oxidation reaction occurs at ~−0.4 V to convert –C═O to –C–O–Na, and a reduction reaction occurs at below −0.5 V to reduce –C–O–Na to –C═O during the discharge process.[12–20] Fig. 2b presents the relationships between the specific capacitance values and charge/discharge current densities. Over the current density range from 0.1 A g^{-1} to 9 A g^{-1}, the samples exhibit outstanding capacitive performance. For example, the calculated specific capacitance (SC) reached 357, 204, 155, 134, 120, 108, and 103 F g^{-1} at a current density of 0.2, 0.4, 1, 2, 4, 5 and 9 A g^{-1}, respectively. The sluggish reduction in SC values suggests an enhanced rate performance. To further explore the kinetic process of Na^+ storage, cyclic voltammograms (CVs) were recorded. As shown in Fig. 2c, a pair of representative redox peaks are observed in similar potential regions during the CV scan at different rates (1–1000 mV s^{-1}). This phenomenon indicates the reversible association/disassociation of Na^+ from the PTCDI framework *via* the enolization reaction (–C═O ↔ –C–O–Na). To further reveal the kinetic information, the relationships between peak currents (i) and scan rates (v) are presented as eqn (9).[23–32]

$$i = av^b \tag{9}$$

Herein the values of a and b are variable. If the value of b is set as 0.5, the kinetic behavior is controlled by diffusion; if the value of b approaches 1, it suggests that the surface-controlled pseudocapacitive behavior is dominant. The value of b can be calculated from the linear relationship between log i and log v. As displayed in Fig. 2d, the values of b for cathodic and anodic peaks are almost equal to each other (0.8277 and 0.7961), further consolidating the satisfactory reversibility for sodium ion accumulation and release. In addition, these two values are close to 1, inferring the dominant contribution of the surface-controlled capacitive behavior. The diffusion and capacitive ratios were further estimated according to eqn (10):[23–32]

$$i = k_1v + k_2v^{1/2} \tag{10}$$

Herein k_1v and $k_2v^{1/2}$ stand for the current caused by the surface-controlled capacitive effect and the diffusion-controlled process respectively. eqn (10) can be further transformed into eqn (11):[23–32]

$$i/v^{1/2} = k_1v^{1/2} + k_2 \tag{11}$$

The diffusion and capacitive ratios can be calculated by plotting $i/v^{1/2}$ *vs.* $v^{1/2}$ at various potentials. As shown in Fig. 2e, about 67% of the total current is derived from capacitive behavior even at 1 mV s^{-1}. Along with the increase of scan rates (1–100 mV s^{-1}), the capacitive contribution is gradually enhanced from 67% to 99% (Fig. 2f). Furthermore, EIS is employed to probe the interfacial contact between the electrode material and electrolyte in the redox process (Fig. S2†). At very high frequencies, the intercept at the real part (Z') is a combinational resistance of the ionic resistance of the electrolyte,

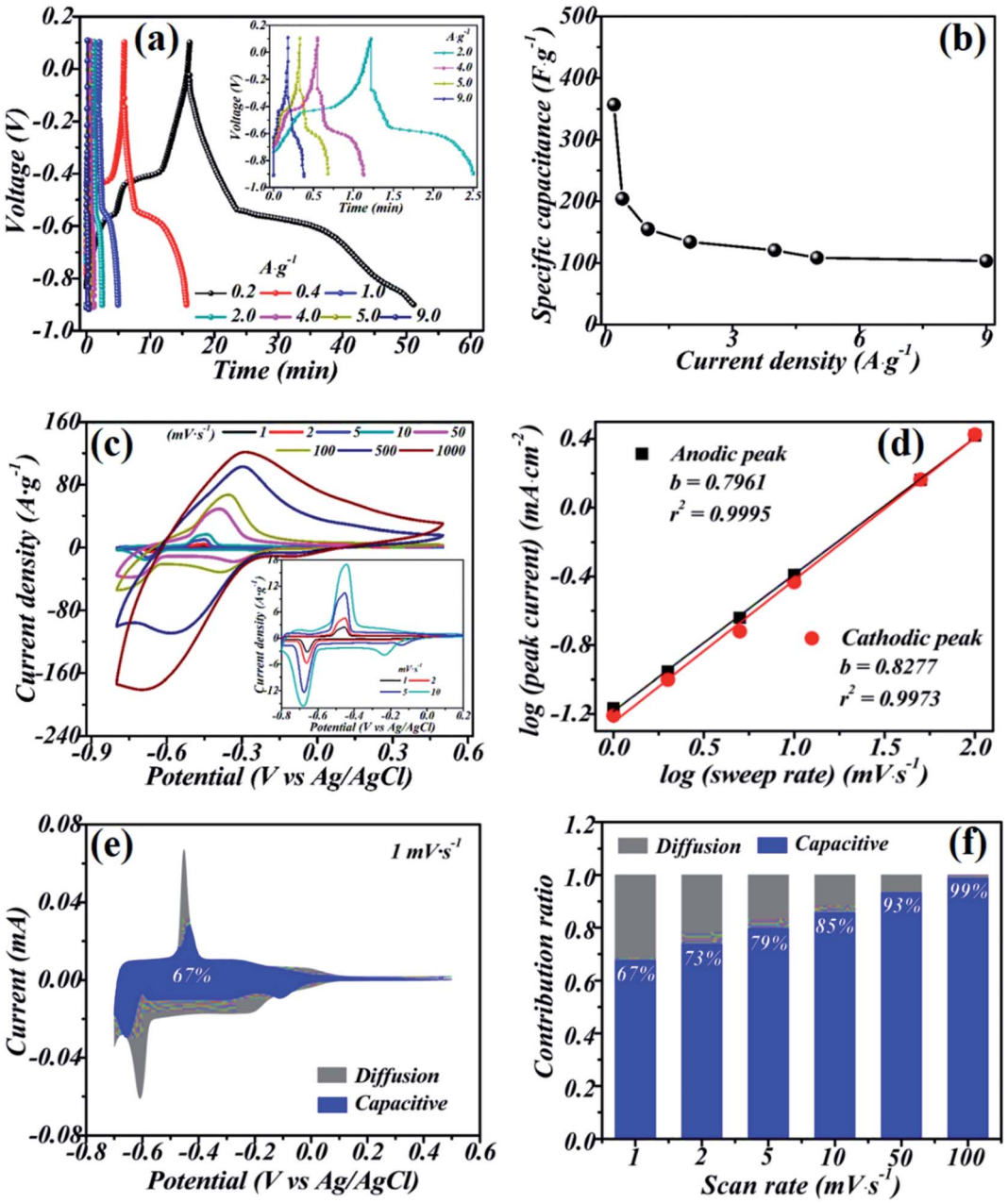

Fig. 2 (a) GCD measurements of the PTCDI nanofiber electrode at different current densities in a 1 M Na_2SO_4 aqueous electrolyte. (b) The relationships between specific capacitances and applied current densities. (c) CV plots of the PTCDI nanofiber electrode at different sweep rates from 1 to 10 000 mV s^{-1}. (d) *b* values calculated from the relationships between the scan rates and peak currents. (e) The proportions of capacitive and diffusion currents in the PTCDI nanofiber electrode at a scan rate of 1 mV s^{-1}. (f) The percentages of capacitive and diffusion-controlled contributions at various sweep rates.

intrinsic resistance of the substrate and contact resistance at the active material/current collector interface (R_S). Here similar R_S values at different voltages are observed (see the inset). A major difference is the semicircle (the smaller the better) in the medium-frequency range, which corresponds to the charge-transfer resistance (R_{CT}) caused by the faradaic reactions. The R_{CT} depends on ion diffusion/transport in the electrolyte to the electrode surface.[34,35] The R_{CT} at redox potentials is smaller than that at OCV, implying a low ionic/charge transfer resistance between the electrolyte and electrode interface, which can also be due to the tight adhesion of the self-assembled PTCDI nanofibers on the ITO surface. Summarizing the results of the GCD, CV and EIS measurements, a desirable rate performance can be obtained from the self-assembled PTCDI nanofiber.

To further probe the structural evolution of PTCDI and the interior storage mechanism, *in situ* Raman spectroscopy was adopted with a three electrode configuration (Fig. S3†), taking advantage of its high sensitivity to organic species and its low scattering cross-section for water solvent. As depicted in Fig. 3a and b, *in situ* Raman spectroscopy was performed at different

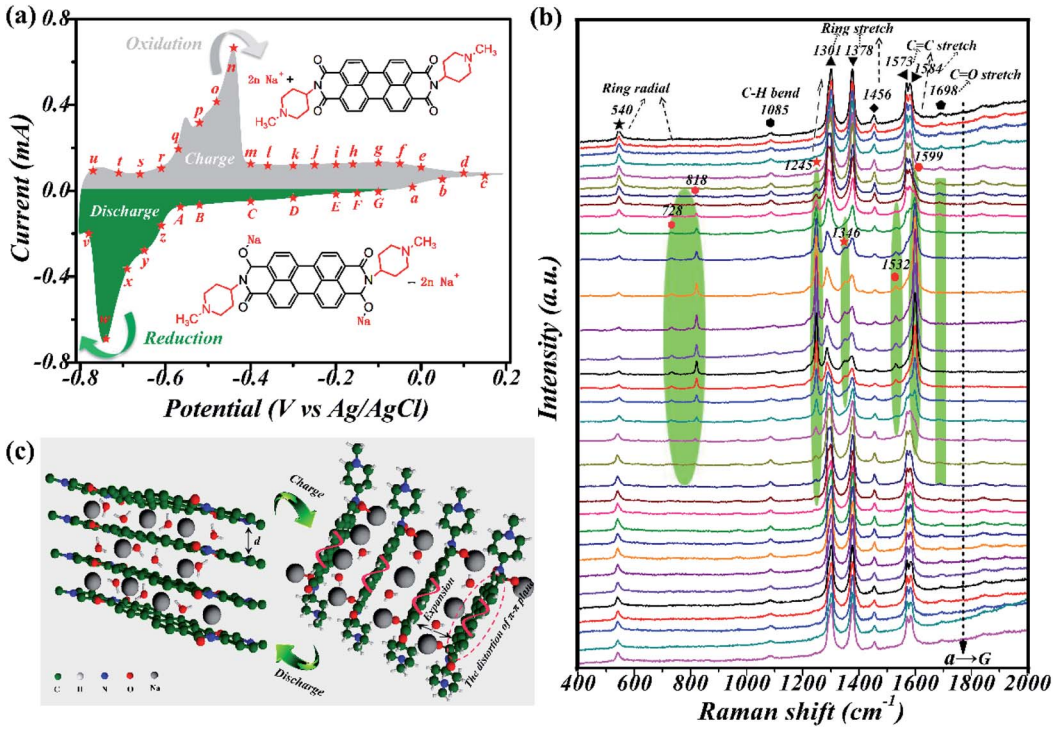

Fig. 3 (a) CV curve of the PTCDI nanofiber electrode at a scan rate of 0.5 mV s^{-1} in a 1 M Na_2SO_4 aqueous electrolyte. (b) The corresponding *in situ* Raman spectroscopic evolution of the PTCDI nanofiber electrode at different applied potentials in CV measurement. (c) The possible structure variations of the PTCDI framework along with the association of Na^+.

potential intervals, during the charge/discharging cycle with a CV scan of 0.5 mV s^{-1}. The peak at 1698 cm^{-1} which is ascribed to the stretching of the C=O group disappears gradually during the oxidation reaction (the gray part in Fig. 3a) and slowly reappears as the reduction reaction proceeds (the blue part in Fig. 3a) within the potential range from 0.2 to −0.8 V, indicating the association/disassociation process of Na^+ *via* a reversible enolization reaction (–C=O ↔ –C–O–Na). Moreover, the appearance/disappearance of the characteristic peaks of the ring radical (Na^+) of PTCDI at 818 and 728 cm^{-1} corresponding to the oxidation/reduction peak in the CV chart further consolidates this transformation reaction. Besides this reaction, the reversibility of structural transformation of PTCDI is also observed *via* the analyses of the C=C stretching and the ring stretching during the charge/discharge process. In detail, the peaks at 1584 and 1573 cm^{-1} which are associated with the C=C stretching mode shift positively to a high wavenumber and merged into one peak at 1599 cm^{-1}, accompanied by the appearance of a satellite peak at 1532 cm^{-1} during oxidating/charging. Reversibly, the peak at 1599 cm^{-1} splits into two peaks of C=C at 1584 and 1573 cm^{-1} along with the fade of the satellite peak (1532 cm^{-1}) during reducing/discharging. Additionally, the ring stretching peaks fluctuate in position and intensity (from 1378/1301 cm^{-1} to 1346/1245 cm^{-1}) during oxidating/charging and restore to the original state during reducing/discharging. This reversibility can also be verified by CV experiments (Fig. S6† and red lines in Fig. 5b), wherein the CV results show high recyclability at different scan speeds (at a low scan rate, the two-step single-electron redox shows two pairs of symmetrical redox peaks in Fig. S6;† while at a high scan rate, it becomes a single-step two-electron redox, showing a pair of symmetrical redox peaks in Fig. 5b), which further proved the reversibility of the structure and reaction. In conclusion, *in situ* Raman spectroscopy indicates the reversible transformation of the structure accompanied by an invertible enolization reaction (–C=O ↔ –C–O–Na). In terms of the molecular structure, four carbonyl groups exist in the symmetric PTCDI molecule, which implies a maximum theoretical capacity of 176 mA h g^{-1} for Na^+ accumulation. However, the actual capacity in our research is only about 110 mA h g^{-1}, which means that only half of the active sites make contributions to the energy storage. To elucidate this discrepancy in capacity and further explore the Na^+ storage mechanism, density functional theory (DFT) calculations were carried out. PTCDI monomers were investigated at the theoretical level of Beck's 3-parameter Lee–Yang–Parr (B3LYP) with the basis set Def2SVP as implemented in Gaussian 09 Rev. D01. It is carried out by simulating the carbonyl reaction at different positions (the carbonyl positions are numbered 1, 2, 3, and 4 in a clockwise direction). As can be seen in Fig. 4a, there are six simulated structures of reactions, namely 1, 1–2, 1–3, 1–4, 1–2–3, and 1–2–3, among which two equivalent Na^+ storage by two carbonyl groups (1–2, 1–3, 1–4) shows lower Gibbs free energy (ΔG); especially the *para* reaction has the smallest Gibbs free energy ($\Delta G = -70$ kcal). This can indicate that the *para*-carbonyl reaction has the greatest spontaneity. In addition, the carbonyl

(a)

Species	Molecular structure	ΔG (kcal/mol)	HOMO (hartree)	LUMO (hartree)	LUMO-HOMO (hartree)
Nomomer-1 Na^+		-58.4	-0.20293	-0.17416	0.02877
Nomomer-1, 2 Na^+		-67.8	-0.29096	-0.24711	0.04385
Nomomer-1, 3 Na^+		-70.5	-0.28803	-0.24894	0.03909
Nomomer-1, 4 Na^+		-65.1	-0.28584	-0.27005	0.01579
Nomomer-1, 2, 3 Na^+		-43.0	-0.35545	-0.3306	0.02485
Nomomer-1, 2, 3, 4 Na^+		+17.8	-0.42841	-0.39129	0.03714

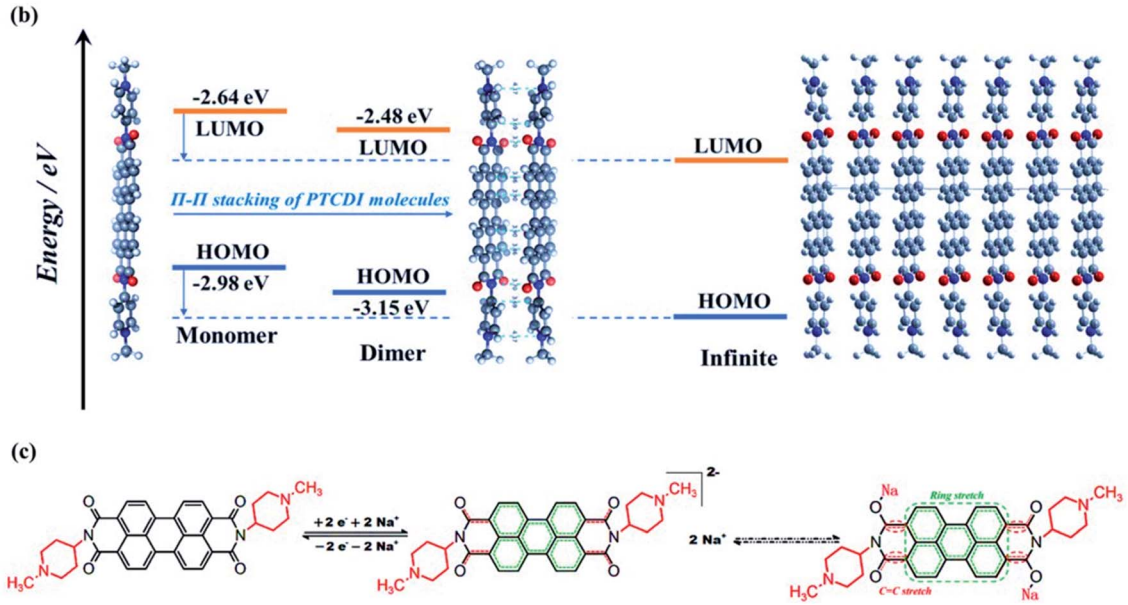

Fig. 4 (a) Gibbs free energies of different reduction sites for the PTCDI monomer. (b) Energy comparison of the HOMO and LUMO orbitals of the PTCDI monomer and dimer. (c) The possible Na^+ storage mechanism of the PTCDI nanofiber electrode.

reactions at positions 1–2 and 1–3 have higher and similar absolute band gap energy, indicating that the products of the reactions at positions 1–2 and 1–3 have relative structural stability. Considering the common influence of Gibbs free energy and absolute band gap energy, it is concluded that the carbonyl reaction products at 1–2 and 1–3 positions coexist, of which the products in 1–3 sites are the main ones. Therefore, the actual capacity is smaller than the theoretical capacity by the simultaneous reaction of four carbonyl groups.[27–29] Furthermore, the energy comparison of the LUMO and HOMO orbitals of the PTCDI monomer and dimer is presented in Fig. 4b. The LUMO/HOMO levels of the PTCDI monomer and dimer were calculated to be −2.64/−2.98 eV and −2.48/−3.15 eV, yielding the absolute energy gaps of 0.34 and 0.67 eV for the PTCDI monomer and dimer, respectively. The higher value indicates that the assembled PTCDI aggregates are more stable than the monomer due to strong π–π interaction.[19,20,27–30] According to the above calculation and the observation in Raman spectra, we proposed the sodium ion storage mechanism as in Fig. 4c.

3.3. Electrochemical characterization of the integrated full cell

To further assess their practical application in flexible electronics, an AFSISD is fabricated, where the PTCDI nanofiber and flexible activated carbon (AC) in Fig. 5a act as the negative electrode and positive electrode respectively. It is envisioned that the utilization of PTCDI will endow the device with a large specific capacitance and correlated high energy density, and the

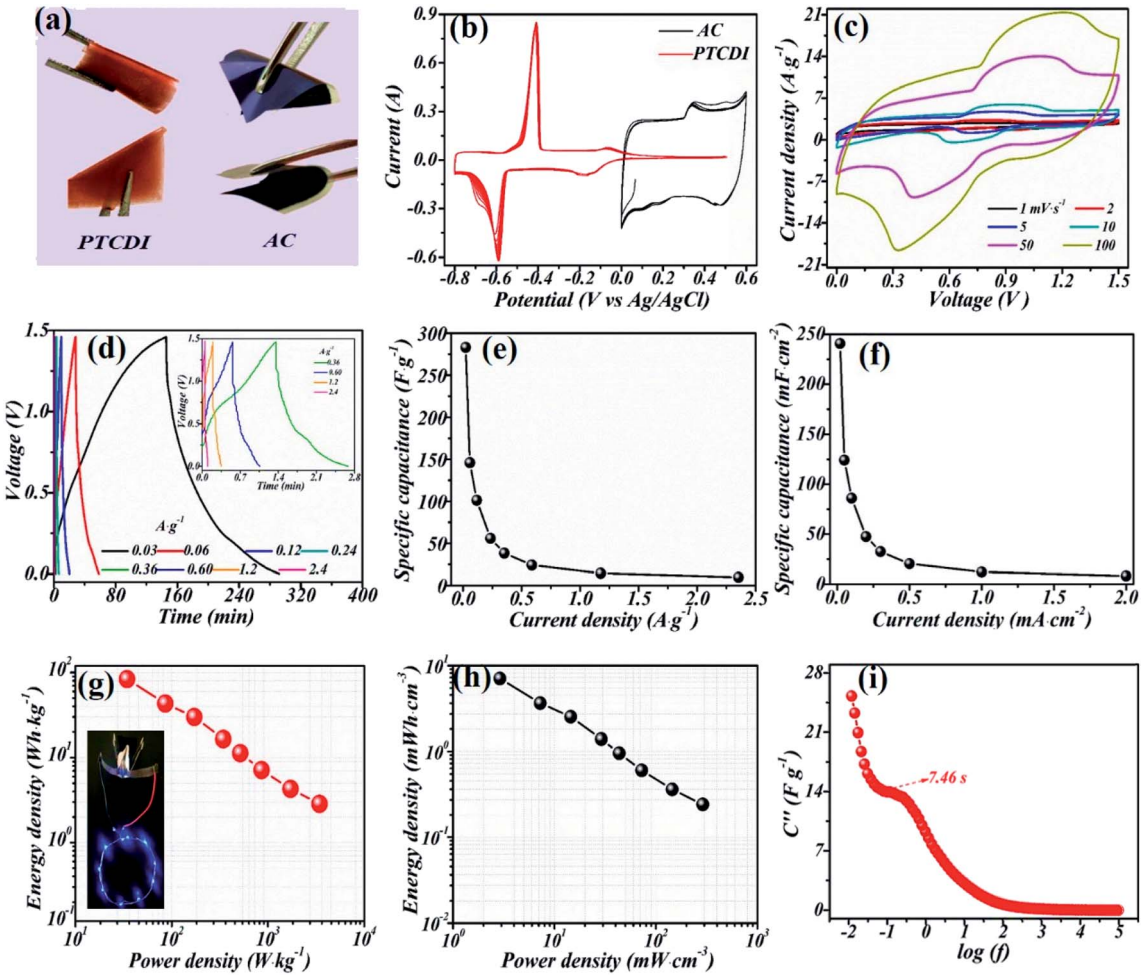

Fig. 5 (a) Photo images of the flexible PTCDI nanofiber electrode and AC electrode. (b) The overlapped CV curves of the PTCDI nanofiber electrode and AC electrode at a scan rate of 5 mV s^{-1} in a 1 M Na_2SO_4 aqueous electrolyte. (c) The CV curves of the PTCDI nanofiber//AC device at the electrode at various scan rates from 1 to 100 mV s^{-1}. (d) GCD measurements of the device at different current densities from 0.03 to 2.4 A g^{-1} (total mass of the cathode and anode was used to calculate current density). (e) The relationships between the mass specific capacitance and applied current density of the FSISD. (f) The relationships between the areal specific capacitance and applied current density of FSISD. (g) and (h) Ragone plots of the FSISD. (i) Frequency dependent imaginary capacitance plot.

participation of AC will endow the device with excellent rate performance, satisfactory power density and a long cycling life. To determine the cut off voltage of the AFSISD, the CVs of the PTCDI nanofiber and AC are overlapped in Fig. 5b. Different from the surface-controlled pseudo-capacitance of Na^+ for the PTCDI nanofiber, a typical double layer capacitance behavior from the adsorption/desorption of SO_4^{2-} ions is found for AC by virtue of its high surface area (2455.8 m^2 g^{-1}) and abundant porosity (Fig. S4 and Table S1†). It is deduced that the maximal cut off voltage for the AFSISD can reach 1.46 V. Moreover, a pair of conspicuous peaks are observed in the CV curves at different scan rates, implying the occurrence of redox reactions during energy storage (Fig. 5c). In addition, the GCD plots demonstrate an enhanced power density (Fig. 5d); for example, the fabricated AFSISD can charge within 35 s at a current density of 2.4 A g^{-1}. As demonstrated in Fig. 5e and f, the maximal mass and areal specific capacitance in the full cell reached 280 F g^{-1} and 241 mF cm^{-2}, respectively, which are higher than those of AC//AC capacitors as shown in Table S2.† Most importantly, benefitting from the cooperation of PTCDI and AC, the AFSISD demonstrates a satisfactory energy and a remarkable power density. As displayed in Fig. 5g and h, the Ragone plots show the overall performance of devices in terms of energy density and power density. It can be seen that a maximal mass energy density of 83.8 W h kg^{-1} and a maximal power density of 3.4 kW kg^{-1} are achieved. The maximal volumetric energy and power densities are 7.1 mW h cm^{-3} and 289.7 mW cm^{-3}, respectively. Furthermore, Fig. 5i demonstrates the relationship between the imaginary capacitance and frequency in electrochemical impedance spectroscopy. A sharp peak and a max capacitance $C''(\omega)$ are obtained at a frequency of f_0 which refers the relaxation time as $\tau_0 = 1/f_0$. The minimum τ_0 is about 7.46 s. This relaxation time manifests the shortest time needed to discharge all the energy from this energy storage device possessing an efficiency of >50%.[31,32] The lower relaxation time also indicates improved power density. Moreover, more than 80% capacity

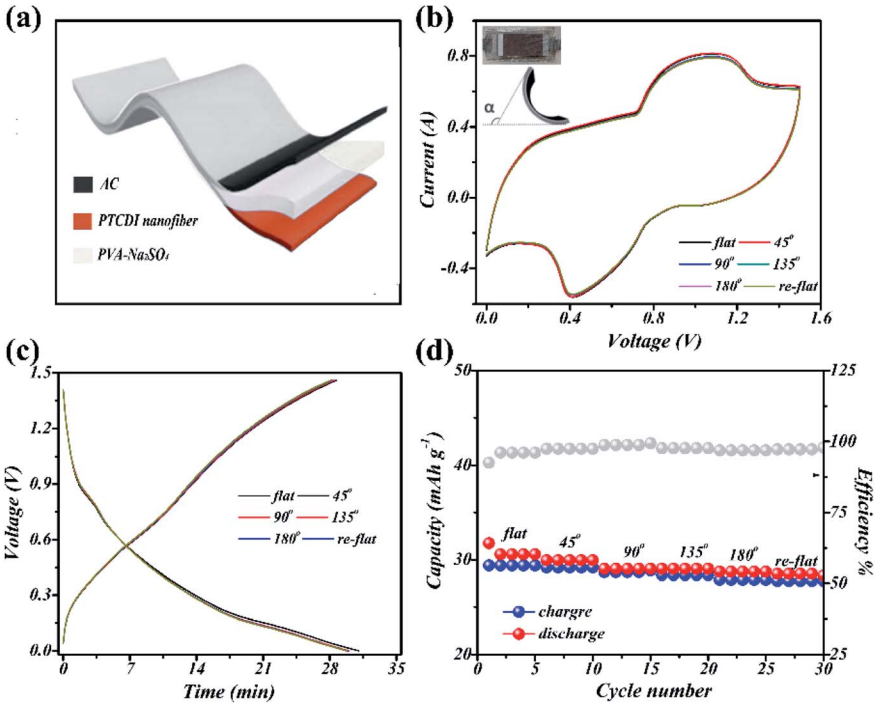

Fig. 6 (a) Schematic illustration of the assembled FSISD; (b) CV curves at a scan rate of 2 mV s^{-1} and (c) the galvanostatic discharge/charge curves of the belt-shaped FSISD at different angles; (d) cycle stability at successive various repeated bending states at a current density of 0.6 A g^{-1}.

retention was obtained at a rapid current density of 0.06 A g^{-1} after 1000 cycles, demonstrating an outstanding cycling stability (Fig. S5, ESI†). Finally, the performance was compared with that of other similar devices. It can be observed from Table S2 (ESI†) that the PTCDI nanofiber//AC device presents desirable overall performance among several proposed aqueous energy storage devices. Such a combination to realize higher energy density and higher power density is expected to bridge the gap between battery-level energy density and supercapacitor-level power density in wearable electronics.

To be used as flexible energy storage devices for powering wearable electronics, mechanical flexibility tests are necessary. As shown in the schematic diagram in Fig. 6a, a flexible quasi-solid-state AFSISD was constructed as a sandwich structure with the PTCDI-nanofiber cathode, AC anode, and poly(vinyl alcohol) (PVA)–Na_2SO_4 gel electrolyte. Fig. 6b exhibits the CV curves of the device at different bending angles, displaying almost imperceptible changes in the coverage areas of the CV curves. Fig. 6c shows the galvanostatic charge/discharge curves for the belt-shaped AFSISD under different bending conditions (initially flat, bending to 45°, 90°, 135°, and 180° and circle to re-flat), and only a minor capacity change occurred under different bending conditions. The corresponding cycling stability results are presented in Fig. 6d. It can be seen that the belt-shaped AFSISD lost a little reversible capacity with repeated bending and continuous different bending operation, which can be attributed to the fact that repeated bending destroyed the tight contact of the anode, separator, and cathode gradually resulting in an increased impedance of the battery. Importantly, the little loss of capacity also demonstrates good flexibility and strong mechanical properties against repeated bending.

4. Conclusions

In conclusion, a PTCDI nanofiber negative electrode was prepared *via* a facile self-assembly strategy. The reversible Na^+ storage mechanism and structural changes for the PTCDI nanofiber were revealed by combining the electrochemical analysis of *in situ* Raman spectroscopy and DFT computation. The pseudo-capacitive behavior based on reversible enolization –C=O ↔ –C–O–Na was demonstrated. The as-prepared PTCDI nanofiber electrode presents desirable Na^+ storage performance, achieving a high capacitance of 357 F g^{-1} at a current density of 0.2 A g^{-1}. Furthermore, a hybrid sodium ion device based on the PTCDI nanofiber as the anode and AC as the cathode was constructed, displaying higher mass energy density (83.8 W h kg^{-1}) and power density (3.4 kW kg^{-1}), and desirable volumetric energy and power densities (7.1 mW h cm^{-3} and 289.7 mW cm^{-3}). Meanwhile, our devices display admirable mechanical flexibility enough to sustain various bending conditions. This work not only push forward the exploration of flexible organic electrodes for energy storage applications, but pioneer research on morphological design for AFSISDs.

Conflicts of interest

The authors declare that they have no conflict of interests.

Acknowledgements

This work was financially supported by the "Western Light" Foundation of Chinese Academy of Sciences (Grant No. 2019-XBQNXZ-A-002), the National Natural Science Foundation of China (Grant No. 51663016), the Youth Innovation Promotion Association, Chinese Academy of Sciences (Grant No. 2019427), the Xinjiang Science Foundation for Distinguished Young Scholars (Grant No. 2019Q004, 2019Q005) and the Xinjiang Program of Introducing High-Level Talents (Grant No. E0398801).

References

1 A. S. Arico, P. Bruce, B. Scrosati, *et al.*, Nanostructured materials for advanced energy conversion and storage devices, *Nat. Mater.*, 2005, **4**, 366–367.
2 B. Dunn, H. Kamath and J. M. Tarascon, Electrical energy storage for the grid: a battery of choices, *Science*, 2011, **334**, 928–935.
3 Y. G. Guo, J. S. Hu and L. J. Wan, Nanostructured materials for electrochemical energy conversion and storage devices, *Adv. Mater.*, 2008, **20**, 2878–2887.
4 D. Larcher and J. M. Tarascon, Towards greener and more sustainable batteries for electrical energy storage, *Nat. Mater.*, 2015, **7**, 19–29.
5 V. Augustyn, P. Simon and B. Dunn, Pseudo-capacitive oxide materials for high-rate electrochemical energy storage, *Energy Environ. Sci.*, 2014, **7**, 1597–1614.
6 V. Palomares, P. Serras, I. Villaluenga, *et al.*, Na-ion batteries, recent advances and present challenges to become low cost energy storage systems, *Energy Environ. Sci.*, 2012, **5**, 5884–5901.
7 X. Dong, L. Chen, X. Su, *et al.*, Flexible aqueous lithium-ion battery with high safety and large volumetric energy density, *Angew. Chem., Int. Ed.*, 2016, **55**, 7474–7477.
8 J. Ding, H. L. Wang, Z. Li, *et al.*, Update on Na-based battery materials: a growing research path, *Energy Environ. Sci.*, 2013, **6**, 2312–2337.
9 B. Häupler, A. Wild and U. S. Schubert, Carbonyls: powerful organic materials for secondary batteries, *Adv. Energy Mater.*, 2015, **5**, 1402034.
10 Y. Liang, Z. Tao and J. Chen, Organic electrode materials for rechargeable lithium batteries, *Adv. Energy Mater.*, 2012, **2**, 742–769.
11 Y. Lu, X. Hou, L. Miao, *et al.*, Cyclohexanehexone with ultrahigh capacity as cathode materials for lithium-ion batteries, *Angew. Chem., Int. Ed.*, 2019, **58**, 7020–7024.
12 L. Zhao, J. Zhao, Y. S. Hu, *et al.*, Disodium Terephthalate (Na2C8H4O4) as high performance anode material for low-cost room-temperature sodium-ion battery, *Adv. Energy Mater.*, 2012, **2**, 962–965.
13 G. Hernandez, N. Casado, A. M. Zamarayeva, *et al.*, Perylene polyimide-polyether anodes for aqueous all-organic polymer batteries, *ACS Appl. Energy Mater.*, 2018, **1**, 7199–7205.
14 C. Wang, W. Tang, Z. Yao, *et al.*, Potassium perylene-tetracarboxylate with two-electron redox behaviors as a highly stable organic anode for K-ion batteries, *Chem. Commun.*, 2019, **55**, 1801–1804.
15 X. Sun, C. Wang, Y. Gong, *et al.*, A flexible sulfur-enriched nitrogen doped multichannel hollow carbon nanofibers film for high performance sodium storage, *Small*, 2018, **14**, 1802218.
16 Z. Wang, H. Li, Z. Tang, *et al.*, Hydrogel electrolytes for flexible aqueous energy storage devices, *Adv. Funct. Mater.*, 2018, **28**, 1804560.
17 H. Li, L. Peng, Y. Zhu, *et al.*, Achieving high-energy–high-power density in a flexible quasi-solid-state sodium ion capacitor, *Nano Lett.*, 2016, **16**, 5938–5943.
18 V. L. Pushparaj, M. M. Shaijumon, A. Kumar, *et al.*, Flexible energy storage devices based on nanocomposite paper, *Proc. Natl. Acad. Sci. U. S. A.*, 2007, **104**, 13574–13577.
19 S. Chen, P. Slattum, C. Wang, *et al.*, Self-assembly of perylene imide molecules into 1D nanostructures: methods, morphologies, and applications, *Chem. Rev.*, 2015, **115**, 11967–11998.
20 L. Yang, M. Wang, P. M. Slattum, *et al.*, Donor-acceptor supramolecular organic nanofibers as visible-light photoelectrocatalysts for hydrogen production, *ACS Appl. Mater. Interfaces*, 2018, **10**, 19764–19772.
21 K. E. Brown, B. S. Veldkamp, D. T. Co, *et al.*, Vibrational dynamics of a perylene-perylenediimide donor-acceptor dyad probed with femtosecond stimulated Raman Spectroscopy, *J. Phys. Chem. Lett.*, 2012, **3**, 2362–2366.
22 M. Angelella, C. Wang and M. J. Tauber, Resonance Raman spectra of a perylene bis(dicarboximide) chromophore in ground and lowest triplet states, *J. Phys. Chem. A*, 2013, **117**, 9196–9204.
23 H. S. Kim, J. B. Cook, H. Lin, *et al.*, Oxygen vacancies enhance pseudocapacitive charge storage properties of MoO3-x, *Nat. Mater.*, 2017, **16**, 454–460.
24 K. J. Stevenson, V. Ozolins and B. Dunn, Electrochemical energy storage, *Acc. Chem. Res.*, 2013, **46**, 1051–1052.
25 T. Brezesinski, J. Wang and S. H. Tolbert, Ordered mesoporous alpha-MoO3 with iso-oriented nanocrystalline walls for thin-film pseudocapacitors, *Nat. Mater.*, 2010, **9**, 146–151.
26 V. Augustyn, J. Come, M. A. Lowe, *et al.*, High-rate electrochemical energy storage through Li+ intercalation pseudocapacitance, *Nat. Mater.*, 2013, **12**, 518–522.
27 N. Zindy, J. T. Blaskovits, C. Beaumont, *et al.*, Pyromellitic diimide-based copolymers and their application as stable cathode active materials in lithium and sodium-ion batteries, *Chem. Mater.*, 2018, **30**, 6821–6830.
28 N. Zindy, C. Aumaitre, M. Mainville, *et al.*, Pyrene diimide based pi-conjugated copolymer and single-walled carbon nanotube composites for lithium-ion batteries, *Chem. Mater.*, 2019, **31**, 8764–8773.
29 J. Wang, W. Shi, D. Liu, *et al.*, Supramolecular organic nanofibers with highly efficient and stable visible light photooxidation performance, *Appl. Catal., B*, 2017, **202**, 289–297.

30 D. Chen, A. J. Avestro, Z. Chen, *et al.*, A rigid naphthalenediimide triangle for organic rechargeable lithium-ion batteries, *Adv. Mater.*, 2015, **27**, 2907–2912.
31 M. Biswal, A. Banerjee, M. Deo, *et al.*, From dead leaves to high energy density supercapacitors, *Energy Environ. Sci.*, 2013, **6**, 1249–1259.
32 J. Yin, Y. Zhu, X. Yue, *et al.*, From environmental pollutant to activated carbons for high-performance supercapacitors, *Electrochim. Acta*, 2016, **201**, 96–105.
33 Z. Zhang, J. Wang, D. Liu, *et al.*, Highly efficient organic photocatalyst with full visible light spectrum through π–π stacking of TCNQ–PTCDI, *ACS Appl. Mater. Interfaces*, 2016, **8**, 30225–30231.
34 N. Wei, L. Ruan, W. Zeng, *et al.*, Compressible supercapacitor with residual stress effect for sensitive elastic-electrochemical stress sensor, *ACS Appl. Mater. Interfaces*, 2018, **10**, 38057–38065.
35 Y. Ma, N. Wei, Q. Wang, *et al.*, Ultrathin PEDOT: PSS/rGO aerogel providing tape-like self-healable electrode for sensing space electric field with electrochemical mechanism, *Adv. Electron. Mater.*, 2019, **5**, 1900637.